Physics of the Earth and Planetary Interiors 274 (2018) 37–48

Contents lists available at ScienceDirect

Physics of the Earth and Planetary Interiors

journal homepage: www.elsevier.com/locate/pepi

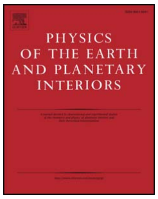

Extension of the energy-to-moment parameter Θ to intermediate and deep earthquakes

Nooshin Saloor[*], Emile A. Okal

Department of Earth & Planetary Sciences, Northwestern University, Evanston, IL, United States

ABSTRACT

We extend to intermediate and deep earthquakes the slowness parameter Θ originally introduced by Newman and Okal (1998). Because of the increasing time lag with depth between the phases *P, pP* and *sP*, and of variations in anelastic attenuation parameters t^*, we define four depth bins featuring slightly different algorithms for the computation of Θ. We apply this methodology to a global dataset of 598 intermediate and deep earthquakes with moments greater than 10^{25} dyn*cm. We find a slight increase with depth in average values of Θ (from -4.81 between 80 and 135 km to -4.48 between 450 and 700 km), which however all have intersecting one-σ bands. With widths ranging from 0.26 to 0.31 logarithmic units, these are narrower than their counterpart for a reference dataset of 146 shallow earthquakes ($\sigma = 0.55$). Similarly, we find no correlation between values of Θ and focal geometry. These results point to stress conditions within the seismogenic zones inside the Wadati-Benioff slabs more homogeneous than those prevailing at the shallow contacts between tectonic plates.

1. Introduction: the slowness parameter Θ

The purpose of this paper is to extend to intermediate and deep earthquakes the calculation of the parameter Θ introduced by Newman and Okal (1998) (hereafter NO98) to characterize the source slowness of shallow earthquakes, allowing in particular the identification of anomalously slow events. NO98 were motivated by the need to detect any possible slowness in the earthquake source with the consequent potential for enhanced tsunami excitation, using an algorithm both robust and fast, in the context of operational tsunami warning (Weinstein and Okal, 2005). This was achieved by comparing quantitative estimates of the earthquake source at low frequencies (seismic moment M_0) and high frequencies (radiated energy E^E), through the parameter

$$\Theta = \log_{10}\frac{E^E}{M_0} \tag{1}$$

This formalism differs from Boatwright and Choy's (1986) in that the estimated energy E^E is computed using an average value of depth and focal mechanism, reflecting the fact that these parameters may not be known exactly under real-time operational conditions. In this respect, the evaluation of Θ shares the general philosophy of a *magnitude* estimate.

In the present study, we extend NO98's methodology to intermediate and deep earthquakes (hereafter "*I*", $80 \leqslant h < 300$ km; and "*D*", $h \geqslant 300$ km, respectively). We are motivated by the documentation, for shallow earthquakes, of a significant diversity in parameters Θ. While seismic scaling laws (Geller, 1976) would predict an invariant value of $\Theta = -4.90$, Fig. 1 documents a subset of shallow events with significant populations featuring deficient values ($\Theta < -5.8$), which correspond to slow earthquakes whose spectra are red-shifted towards low frequencies. They include all so-called "*tsunami earthquakes*" whose tsunamis are significantly larger than predicted by their seismic magnitudes, especially conventional ones (Kanamori, 1972), generally as a result of low rupture velocities (Tanioka et al., 1997; Polet and Kanamori, 2000). On the other hand, Fig. 1 also shows a number of events with enhanced values, indicating a spectrum blue-shifted towards high frequencies, usually under the influence of a short source duration. We refer to such earthquakes as "snappy" events, which can feature higher ground accelerations and therefore exceptional levels of destruction as exemplified by intraplate shocks such as the 2011 event in Christchurch ($\Theta = -4.19$) and the large 1939 Chillán, Chile earthquake (Okal and Kirby, 2002, $\Theta = -4.04$).

Such variations in energy-to-moment ratio for shallow earthquakes, which reflect diversity in tectonic environments, have been described, notably by Choy and Boatwright (1995) and Choy et al. (2006). They can extend over 3 logarithmic units and cast Θ as a "slowness parameter", a name first introduced by Weinstein and Okal (2005). By extending the computation of Θ to intermediate and deep earthquakes, we seek to explore any potentially similar diversity; we conclude that these

---

[*] Corresponding author.

E-mail address: nooshin@earth.northwestern.edu (N. Saloor).

http://dx.doi.org/10.1016/j.pepi.2017.10.006
Received 6 May 2017; Received in revised form 17 October 2017; Accepted 22 October 2017

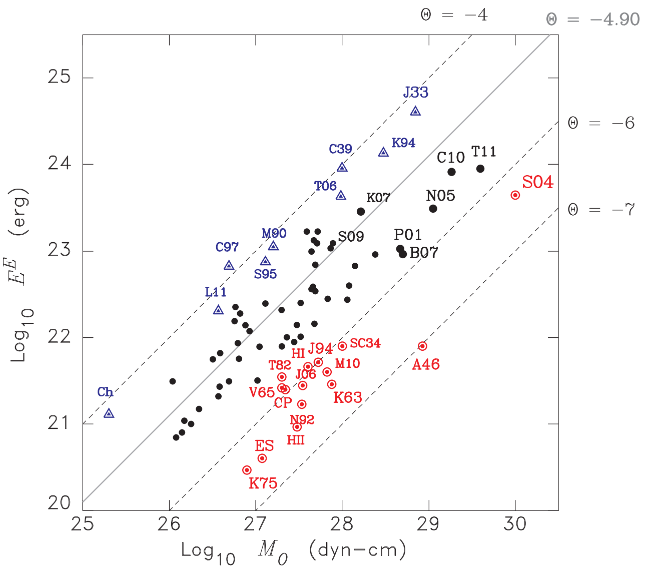

Fig. 1. Plot of the estimated energy, E^E vs. seismic moment M_0 for shallow events, updated from the original work of Newman and Okal (1998). Previously studied tsunami earthquakes ($\Theta < -5.8$) are shown as red bull's eye symbols (SC34, Santa Cruz, 1934; A46, Aleutian 1946; HI and HII, Hikurangi, 1947; K63, Kuril 1963; V65, Vanuatu 1965; K75, Kuril 1975; T82, Tonga 1982; N92, Nicaragua 1992; J94, Java 1994; CP, Chimbote, Peru 1996; S04, Sumatra, 2004; J06, Java 2006; M10, Mentawai 2010; ES, El Salvador, 2012) The blue triangles ($\Theta > -4.3$) identify "snappy" earthquakes (J33, Sanriku, 1933; C39, Chillán 1939; M90, Marianas 1990; K94, Kuril 1994; S95, Samoa 1995; C97, Chile 1997; T06, Tonga 2006; Ch, Christchurch 2011; L11, Loyalty Is. 2011), and the black dots regular events (P01, Peru 2001; N05, Nias 2005; B07, Bengkulu 2007; K07, Kuril 2007; S09, Samoa 2009; C10 Chile 2010; and T11, Tohoku 2011).

deeper sources have much more homogeneous properties in this respect.

2. Methodology

While the general approach to the computation of energy flux and hence E^E and Θ is unchanged for deeper sources, significant changes will be required in the details of the algorithm, which carried implicit assumptions on the seismic rays and structural parameters involved. In order to identify those changes, we examine in detail the various steps in NO98's algorithm for the computation of E^E for shallow events, itself derived from Boatwright and Choy (1986).

a. First, an energy flux ε is calculated at a teleseismic station as twice the integral over time of the density of kinetic energy, multiplied by the local *P*-wave velocity α (Wu, 1966):

$$\varepsilon = \rho\ \alpha \int_0^\infty \dot{u}^2(t)\ dt \tag{2}$$

where u is the vertical ground motion (assumed deconvolved from instrument response), and ρ the local crustal density. In practice, this time-domain integral is limited to the duration of the *P* wavetrain, t_{max}. In the case of shallow events, the so-called generalized *P* wave includes the source-reflected *pP* and *sP* which cannot be separated from direct *P*. As discussed more in detail below, t_{max} will have to be modified in the case of *I* or *D* sources.

b. Next, using Parseval's theorem, Eq. (2) is transformed to the frequency domain

$$\varepsilon^* = \frac{\rho\alpha}{\pi} \int_0^\infty |\omega.\ u(\omega)|^2 \exp\left[\omega t^*(\omega)\right]\ d\omega \tag{3}$$

In practice, the integral is computed between the finite bounds $\omega_{min} = 2\pi/10$ and $\omega_{max} = 2\pi/0.5$ rad/s. We include in (3) a correction for anelastic attenuation along the ray path, expressed through the parameter

$$t^* = \int_{path} \frac{Q^{-1}}{v(r)}\ ds \tag{4}$$

where Q^{-1} is intrinsic attenuation, and $v(r)$ the local seismic velocity along the path. For shallow sources, it has long been assumed (Carpenter, 1965) that t^* can be taken as independent of distance, and approximately equal to 1 s for *P* waves (and 4 s for *S* waves). This reflects the fact that the principal contribution to the integral (4) comes from the asthenosphere, where attenuation is significantly higher than in the upper and lower layers of the mantle (Anderson and Hart, 1978). For shallow events, there are two such transits, source-side and receiver-side, largely independent of distance, leading to constant t^*. However, $t^* = 1$ s has later been found to overestimate attenuation (Anderson and Given, 1982; Choy and Cormier, 1986), which motivated Choy and Boatwright (1995) and NO98 to use the frequency-dependent expression (t^* in s and f in Hz):

$$\begin{aligned} t^* &= 0.9\text{–}0.1\ \log_{10} f \quad (f \leqslant 0.1\ \text{Hz}) \\ t^* &= 0.5\text{–}0.5\ \log_{10} f \quad (0.1 \leqslant f \leqslant 1\ \text{Hz}) \\ t^* &= 0.5\text{–}0.1\ \log_{10} f \quad (f \geqslant 1\ \text{Hz}), \end{aligned} \tag{5}$$

based on the work of Choy and Cormier (1986) and Choy and Dewey (1988).

By contrast, for intermediate and deep sources, direct *P* may undergo only one such transit while the situation with reflected phases is much more complex, since their upswing parts may or may not benefit from a low attenuation path by riding up the slab. Detailed values of t^* used in this study will be discussed in Section 2.1.

c. Next, the energy flux ε^* is scaled back to a focal sphere of unit radius, using the concept of geometrical spreading

$$\varepsilon^*_{FS} = (R^P)^2\ \varepsilon^* \tag{6}$$

where $R^P = a/g(\Delta)$, with a the Earth's radius and the geometrical spreading coefficient $g(\Delta)$ obtained from the travel time of *P* waves $T(\Delta,h)$ as:

$$g(\Delta) = \sqrt{\frac{\rho_h \alpha_h}{\rho_0 \alpha_0}.\ \frac{\tan i_h}{\cos i_0}\ \frac{v_h}{r_h} \left|\frac{d^2T}{d\Delta^2}\right|} \tag{7}$$

adapted, e.g., from Okal (1992). In the NO98 algorithm, this is calculated directly from a tabulated version of the Jeffreys-Bullen tables. It can be adapted seamlessly to the case of intermediate and deep sources.

d. Finally, a focal mechanism correction is then effected, in order to restore the full energy radiated by the double-couple into *P* waves, rather than measured from the generalized *P* wave (*gP*) in a single direction. The energy radiated by a double-couple, integrated over the whole focal sphere, amounts to an average radiation coefficient of *P* waves $<(F^P)^2> = 4/15$. As discussed by Boatwright and Choy (1986), the energy in *gP* can be described through a generalized radiation coefficient expressing the sum of the energy carried by the three rays, *P*, *pP* and *sP*:

$$(F^{gP})^2 = (F^P)^2 + (\acute{P}\grave{P}.\ \ F^{pP})^2 + \frac{2\alpha}{3\beta}\ q\ (\acute{S}\grave{P}^{BC}.\ F^{sP})^2 \tag{8}$$

where all terms are detailed in NO98. The final energy radiated into *P* waves is then obtained as:

$$E^P = 4\pi\ \frac{\langle (F^P)^2 \rangle}{(F^{gP})^2}\ \varepsilon^*_{FS} \tag{9}$$

In the context of the calculation of estimated energy E^E, which ignores the exact depth and focal mechanism, NO98 replaced $(F^{gP})^2$ with its average over focal geometries, regressed with distance Δ (in degrees) as:

$$(F^{Est.})^2(\Delta) = 1.171\text{–}7.271 \times 10^{-3}\Delta + 6.0009 \times 10^{-3}\Delta^2 \tag{10}$$

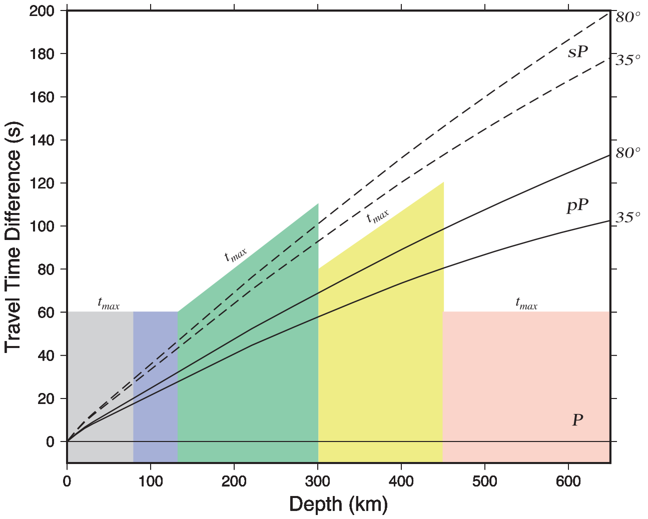

Fig. 2. Travel-time delays of reflected *pP*(solid) and *sP* (dashed) with respect to direct *P* as a function of source depth, for $35° < \Delta < 80°$. The shaded blocks illustrate the lengths of the time series used to compute Θ in the various depth ranges. See text for details.

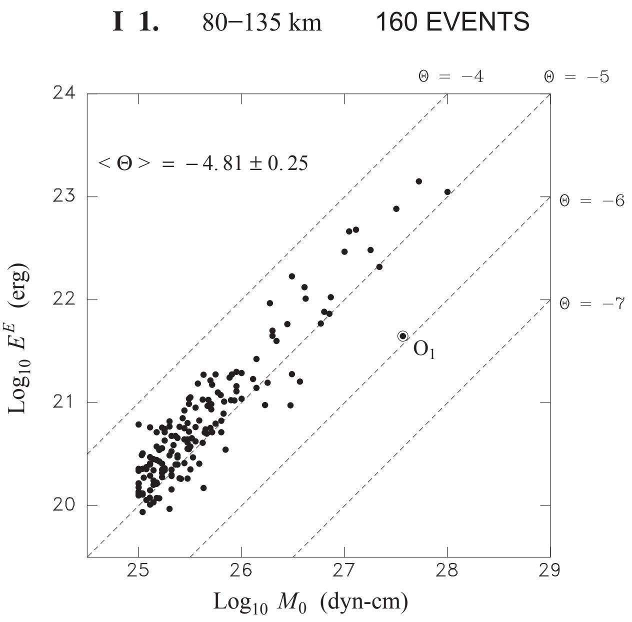

Fig. 3. Plot of estimated energy E^E *vs.* seismic moment M_0, at depths between 80 and 135 km. Lines of constant Θ are shown as dashed lines. O_1 represents the slow outlier in the Solomon Islands subduction system.

Replacing (8) with (10) and adding the contribution of *S*-wave radiation at the source, the estimated energy E^E is then defined as:

$$E^E = \frac{1+q}{4\pi} \frac{\langle (F^P)^2 \rangle}{(F^{Est.})^2} \cdot \ \varepsilon^*_{FS} \qquad (11)$$

and Θ is obtained from (1) by using a published value of M_0 (or an estimated one in real time). A final Θ is retained by averaging values obtained at many stations, this procedure serving to correct for the use of the estimated radiation coefficient (10) rather than the exact one (8) at each station.

In summary, in order to compute E^E and Θ for non-shallow earthquakes, steps **a.** (t_{max}), **b.** (t^*) and **d.** (F^{gP}) will have to be adapted to the particular depth range involved. These adjustments to the algorithm of NO98 are now discussed in detail.

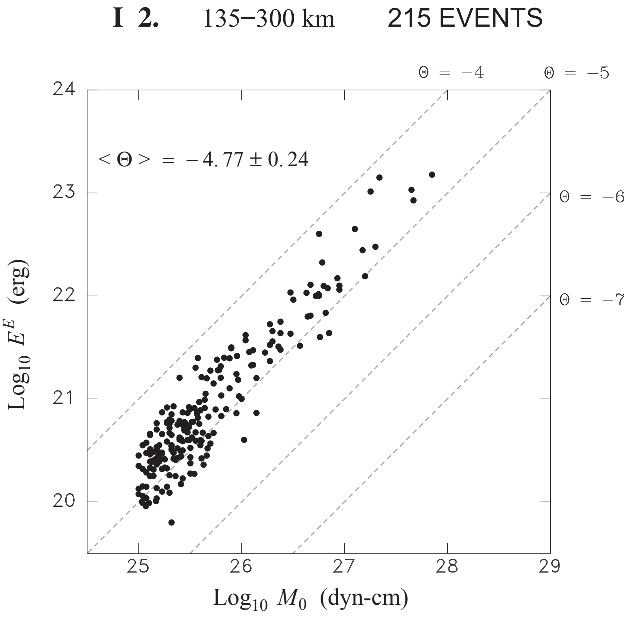

Fig. 4. Same as Fig. 3 for the I – 2 dataset (135–300 km).

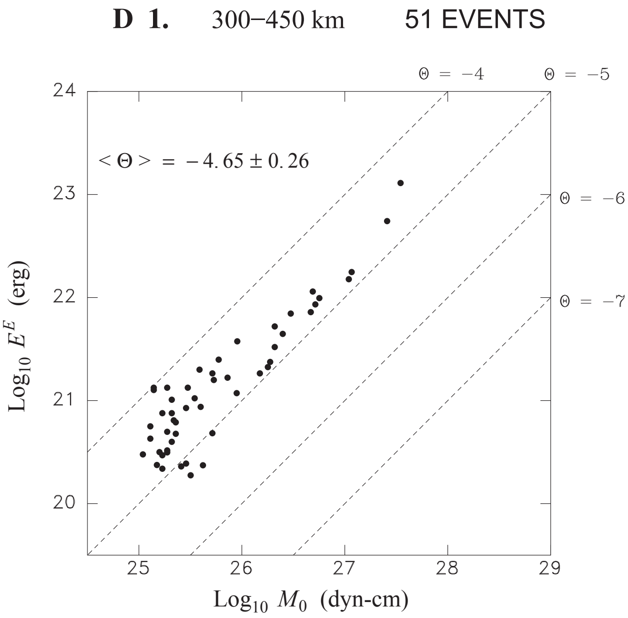

Fig. 5. Same as Fig. 3 for the D – 1 dataset (300–450 km).

2.1. Selection of t_{max}

Fig. 2 plots the travel time differential of the reflected phases *pP* and *sP* with respect to direct *P* as a function of source depth. The grey block at left symbolizes the window used by NO98 for shallow events (0–80 km), starting 10 s before *P* and extending for t_{max} = 70 s (Larger events are given a longer window). In this context we split intermediate and deep earthquakes into four categories, according to depth:

- **Depth Bin I–1: 80 < *h* < 135 km**
  In this depth range, the reflected phases *pP* and *sP* stay within the 70-s time window used for shallow earthquakes, which thus remains adequate for the computation of the energy flux.

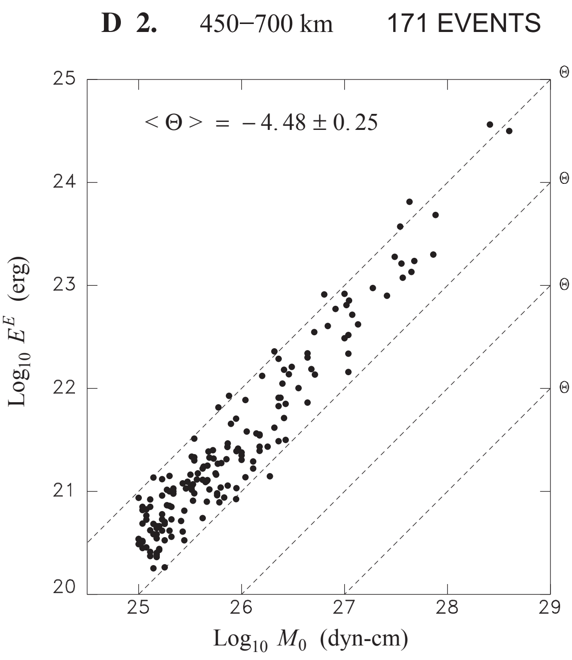

Fig. 6. Same as Fig. 3 for the D – 2 dataset (450–700 km).

∗Depth Bin I–2: 135 < *h* < 300 km

The reflected phases now extend beyond 60 s following first arrival, but are not adequately separated from direct *P*, mandating the use of a depth-dependent t_{max}:

$$t_{max} = 70 + 0.3 \times (h{-}135) \qquad (12)$$

(t_{max} in s and h in km).

∗Depth Bin D–1: 300 < *h* < 450 km

In this depth range, the shear-reflected phase *sP* becomes adequately separated from *pP* and the computation can proceed using only direct *P* and *pP*, with:

$$t_{max} = 90 + \frac{(h{-}300)}{5} \qquad (13)$$

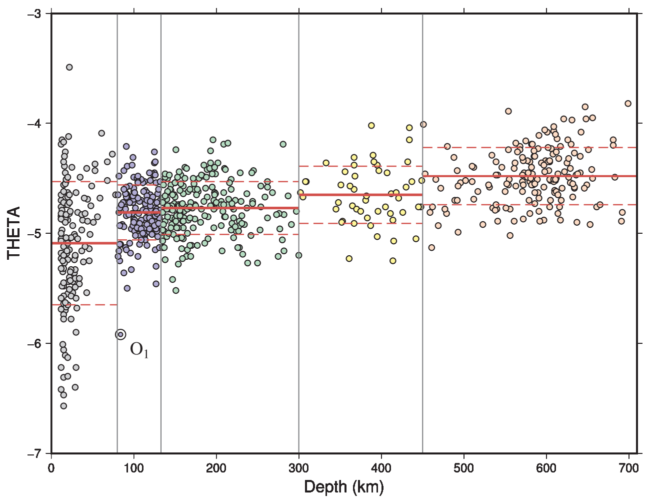

Fig. 7. Cumulative plot of Θ for all depths categories (0–700 km). Average values of Θ and their one-σ bands are shown in red (solid and dashed segments), respectively. Note that shallow events are much more scattered than intermediate and deep ones. The outlier O_1 is identified by a bull's eye symbol.

(t_{max} in s and h in km).

∗Depth Bin D–2: 450 < *h* < 700 km

Both reflected phases are now well separated from direct *P* with *pP* arriving more than 80 s after the first arrival. The computation can proceed on direct *P* only, reverting to t_{max} = 70 s.

In this context, we wish to stress, as initially pointed out in NO98, that the Θ algorithm proceeds in the general scope of a *magnitude* computation, which in particular ignores such details as focal mechanism and exact depth (through the simple use of four depth classes). More sophisticated algorithms have been implemented, such as Choy and Boatwright's (1995), who use a time window (t_{max}) customized to each seismogram, depending on the fall-off of Direct *P* with time (Choy and Dewey, 1988). This difference in methodology may lead to disparities in energy values, for example under the scenario of a complex, jagged rupture, with a series of delayed small events.

Table 1
Summary of results.

Intermediate and Deep

Depth Bin	Standard dataset		Other datasets					
	N_{min} = 10		N_{min} = 1		N_{min} = 20		N_{max} = 9	
	N_{eq}	<Θ > ± σ	N_{eq}	<Θ > ± σ	N_{eq}	<Θ > ± σ	N_{eq}	<Θ > ± σ
I – 1	160	−4.81 ± 0.25	184	−4.79 ± 0.27	124	−4.84 ± 0.26	24	−4.65 ± 0.32
I – 2	216	−4.77 ± 0.24	255	−4.77 ± 0.25	178	−4.77 ± 0.25	39	−4.76 ± 0.29
D – 1	51	−4.65 ± 0.26	57	−4.63 ± 0.26	43	−4.65 ± 0.27	6	−4.53 ± 0.18
D – 2	171	−4.48 ± 0.26	195	−4.48 ± 0.26	135	−4.49 ± 0.24	25	−4.50 ± 0.33
All four bins	598	−4.69 ± 0.29	691	−4.68 ± 0.29	480	−4.70 ± 0.29	93	−4.65 ± 0.32

Shallow reference dataset

	N_{eq}	<Θ > ± σ
Global	146	−5.10 ± 0.55
Interplate	111	−5.23 ± 0.55
Intraplate	35	−4.68 ± 0.33

Table 2
Influence of focal mechanism on population of Θ.

Mechanism Type	Number of Events	Average Θ	Standard deviation σ
	Intermediate I-1: 80–135 km		
SS	16	−4.88	0.30
NO	30	−4.63	0.28
TH	40	−4.72	0.30
HY	74	−4.65	0.27
	Intermediate I-2:135–300 km		
SS	13	−5.04	0.24
NO	41	−4.78	0.22
TH	64	−4.65	0.23
HY	98	−4.81	0.22
	Deep D-1: 300–450 km		
SS	1	−5.25	
NO	19	−4.61	0.30
TH	2	−4.71	0.18
HY	29	−4.56	0.22
	Deep D-2: 450–700 km		
SS	4	−4.39	0.25
NO	67	−4.49	0.26
TH	10	−4.48	0.27
HY	90	−4.48	0.25
	All Depths: 80–700 km		
SS	34	−4.88	0.30
NO	157	−4.63	0.28
TH	116	−4.72	0.30
HY	291	−4.69	0.27

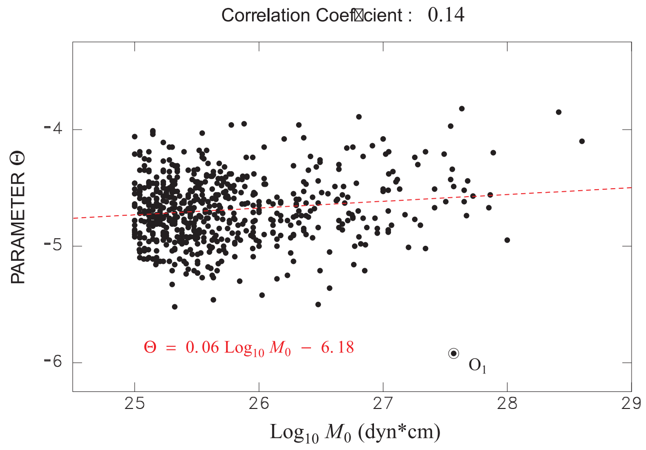

Fig. 8. Whole dataset of 597 intermediate and deep earthquakes. The dashed line is the best regression. Note the insignificant slope and poor correlation coefficient. The outlier O_1 is identified by a bull's eye symbol.

2.2. *Selection of t^**

While a constant value of $t^* = 1$ s constitutes a simple but robust approximation to the effect of attenuation on teleseismic *P* waves from shallow sources, it is clear that it cannot be applied at all depths. We note that for deep sources around 600 km and the phase Direct *P*, Choy and Cormier (1986) have proposed a model (their Fig. 8) which can be approximated by applying to (5) a multiplicative factor of 0.55, as originally proposed by Burdick and Helmberger (1974). This comes close to halving the shallow estimate of t^*, a sensible proposition since rays from such sources undergo only one transit through the upper mantle, rather than two for shallow sources. In other depth bins, the situation is much more complex since t^* will be path-dependent, as direct *P* and *a fortiori* the reflected phases *pP* and *sP* to individual stations may travel through a high-*Q* slab segment, or through strongly attenuating structures in the mantle wedge and back arc (e.g., Roth et al., 1999) for which appropriate three-dimensional models may not be available in all tectonic regions.

In this context, we take the empirical approach of using, in various depth ranges, a t^* model simply applying a multiplicative factor varying with depth to a slightly modified version of Eq. (5):

$$t^* = \gamma(h)\ [0.9\text{–}0.1\ \log_{10} f] \quad (f \leqslant 0.1\ \text{Hz})$$
$$t^* = \gamma(h)\ [0.4\text{–}0.6\ \log_{10} f] \quad (0.1 \leqslant f \leqslant 1\ \text{Hz})$$
$$t^* = \gamma(h)\ [0.4\text{–}0.1\ \log_{10} f] \quad (f \geqslant 1\ \text{Hz}), \tag{14}$$

with $\gamma = 0.55$ in Depth Bin D – 2, $\gamma = 0.6$ in D – 1, $\gamma = 0.75$ between 200 and 300 km, and $\gamma = 0.80$ between 80 and 200 km. This admittedly *ad hoc* model of t^* provides compatibility with Choy and Cormier's (1986) model for deep (D–2) events; in addition, we have verified that it leads to an average $t^* = 0.27$ s used in the integral (3) for D–2 events, in agreement with the value of $t^* \approx 0.3$ s proposed in a number of recent investigations (e.g., Ye et al., 2013; Poli and Prieto, 2016). Finally, note that the use of a large number of stations diversely sampling the hypocentral area should empirically guard against the influence of an inadequate attenuation correction along an individual path.

2.3. *Selection of $\langle (F^{gP})^2 \rangle$*

As in the case of shallow earthquakes (NO98), the value of the estimated generalized radiation coefficient $\langle (F^{gP})^2 \rangle$, is obtained by regressing with distance the expression (8), computed for a large number of combinations of actual sources, drawn from the GlobalCMT catalog (Dziewonski et al., 1981; Ekström et al., 2012), and stations of the Global Seismographic Network. For intermediate depth earthquakes (I – 1 and I – 2), we replace (10) with

$$(F^{Est.})^2(\Delta) = 0.8450 + 3.701 \times 10^{-3}\Delta - 4.335 \times 10^{-5}\Delta^2 \tag{15}$$

(Δ in degrees).

In the D – 1 depth range (300–450 km), where we do not include the shear reflected *sP*, (8) is replaced with

$$(F^{gP})^2 = (F^P)^2 + (\acute{P}\grave{P}.\ F^{pP})^2 \tag{16}$$

which regresses as:

$$(F^{Est.})^2(\Delta) = 0.2353 + 4.109 \times 10^{-3}\Delta - 8.453 \times 10^{-6}\Delta^2 \tag{17}$$

(Δ in degrees).

Finally, for the D – 2 depth range (450–700 km) where we process only direct *P*, we use $(F^{Est.})^2 = 4/15$ as the estimate of the average radiation coefficient.

The radiated energy computed using the above algorithm, and its ratio to seismic moment, can be interpreted under the simple model of a trapezoidal source time function and homogeneous slip on a simple fault plane (Vassiliou and Kanamori, 1982). Under this model, NO98 showed (their Eq. (14)) that the ratio E^E/M_0 was controlled by the strain released (itself the ratio of seismic slip to fault width) and the velocity of rupture V_R along the fault, with a minor dependence on the ratio of rise time to rupture time (or source duration). In turn, E^E/M_0 will be proportional to stress drop Δσ and to apparent stress under Orowan's (1960) conditions. This simple interpretation is generally upheld in the case of shallow earthquakes for which events with deficient Θ, such as tsunami earthquakes, have been documented to feature slow rupture velocities (e.g., Polet and Kanamori, 2000; López and Okal, 2006) and those with enhanced Θ anomalously large displacements, and hence strains (e.g., Beavan et al., 2011). By contrast, in the case of a jagged rupture featuring a series of asperities rupturing in a delayed pattern, the energy-to-moment ratio may keep a regular value, while the rupture velocity averaged over the whole source process would appear deficient.

3. Data selection

Our data selection followed the criteria of NO98: In each of the four

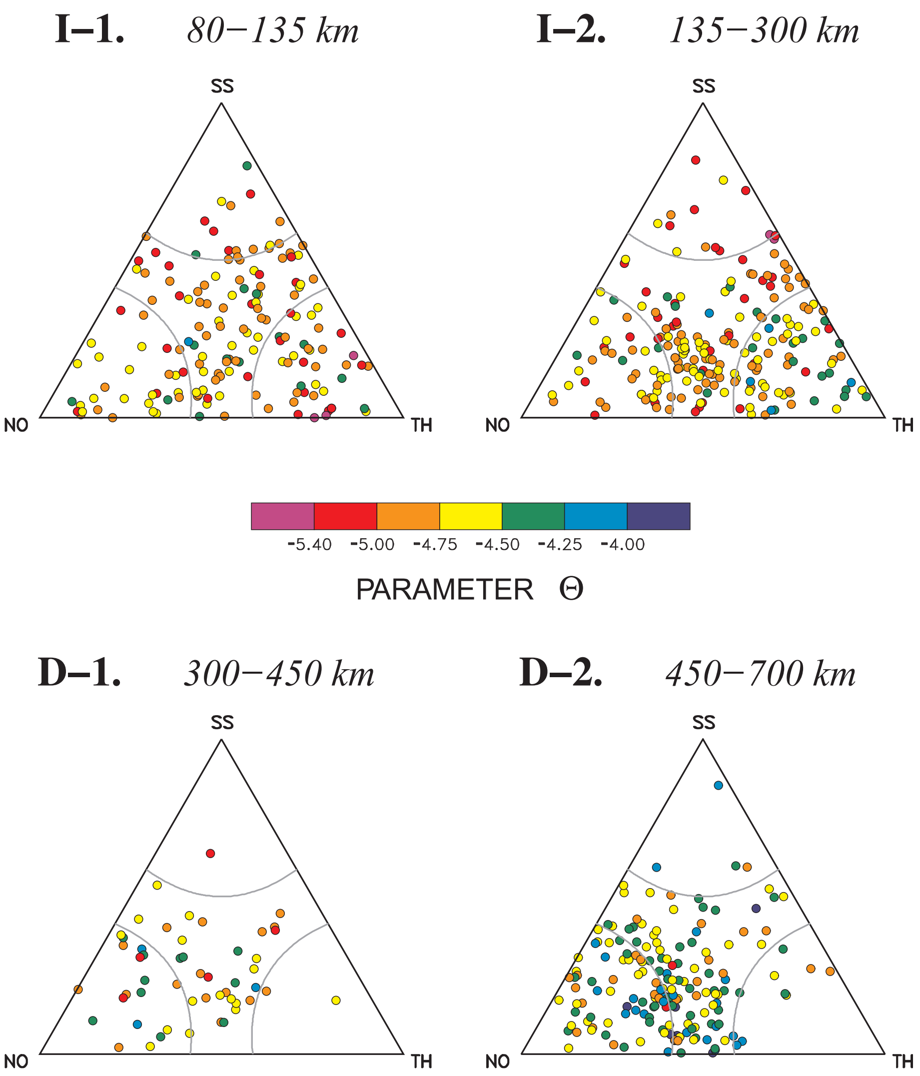

Fig. 9. Ternary diagrams for the four depth bins. Note the absence of any systematic correlation between Θ and focal mechanism.

depth bins, we considered all earthquakes with moments $M_0 > 10^{25}$ dyn∗cm ($M_w > 5.9$; to ensure adequate signal-to-noise ratio), occurring during the years 1990–2016 (to secure a sufficient dataset of digital stations), with seismic moments obtained from the GlobalCMT catalog (Dziewonski et al., 1981; Ekström et al., 2012). We used records from broadband channels of the Global Seismographic Network, sampled at 20 Hz, with epicentral distances $35° < \Delta < 80°$, thus avoiding complexities due to triplication in the mantle, and interaction with D'', respectively. While it is in principle possible to adapt the computation of Θ to shorter or greater distances (Ebeling and Okal, 2012; Okal and Saloor, 2017), this was not deemed necessary here, on account of a sufficiently large number of stations. In this respect, we imposed a minimum of 10 stations per event; the retained dataset then featured an average of 27 stations per event. The insignificant effect, on all our results, of using a different minimum number of stations is discussed in detail in Section 4.1.

In addition, we restricted ourselves to permanent stations of the Global Seismographic Network (mainly the networks IU, II and G, occasionally GE, of the Federation of Seismic Networks), excluding systematically such datasets as the United States Transportable Array. In this fashion, we seek to achieve a balanced distribution of stations on the focal sphere, and to guard against the systematic bias that could be introduced, for example when a massive number of stations would be located close to a node of radiation pattern, as was described in the parallel case of mantle magnitudes by Weinstein and Okal (2005).

Our final dataset includes 160 I – 1 events (80–135 km), 216 I – 2 events (135 – 300 km), 51 D – 1 events (300–450 km) and 171 D – 2 events (450–700 km), for a grand total of 598 non-shallow earthquakes. These numbers reflect the general distribution of seismicity with depth (e.g., Frohlich, 2006, Chapter 4). The full dataset is listed in Table A1 (Supplementary material), including an additional 93 events with fewer than 10 stations, which were discarded from the final dataset. For reference, we also include in our analysis a dataset of 146 shallow earthquakes from the digital era, similarly listed in Table A2 (Supplementary material).

4. Results and discussion

Results for the various depth classes are presented in Figs. 3–6, with Table 1 listing all relevant statistical parameters, including for the reference dataset of 146 shallow earthquakes. Fig. 7 regroups the values of Θ as a function of depth for the whole dataset. While a large amount of literature exists on the subject, initially suggesting that intermediate and deep earthquakes feature higher stress drops and apparent stresses than shallow ones (e.g., Wyss and Molnar, 1972; Fukao and Kikuchi, 1987; Choy et al., 2006), there is no quantitative consensus on such variations (e.g., Frohlich, 2006), with a number of recent studies suggesting comparable apparent stresses at all depths (e.g., Vallée, 2013; Poli and Prieto, 2016). In this context, our homogeneous dataset of 744 Θ values brings additional insight into the behavior of energy-to-moment ratios with depth.

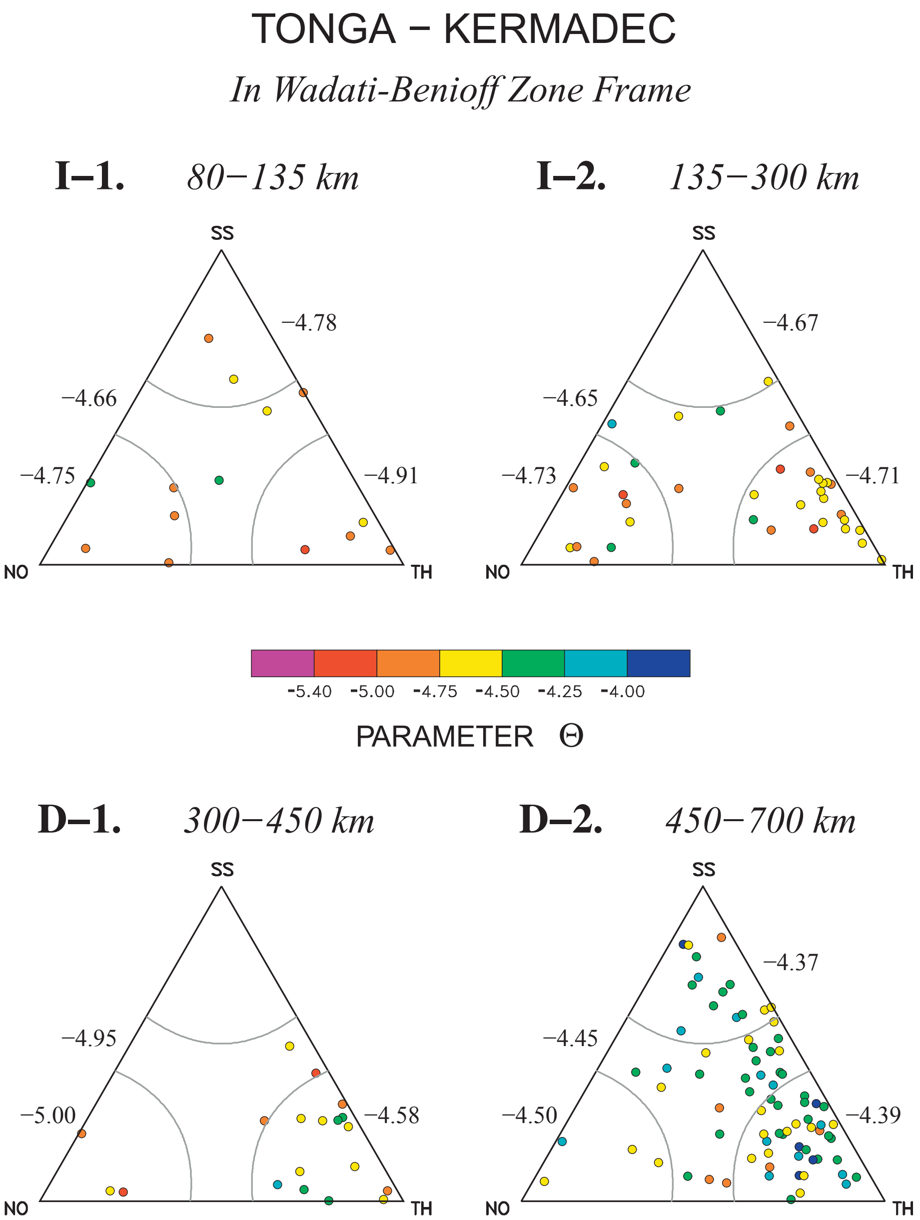

Fig. 10. Same as Fig. 9 for the Tonga-Kermadec subset, after rotation into the frame of the subducting Wadati-Benioff plane. The average values for the 15 combinations of depth bins and focal geometries are shown adjacent to the relevant domains.

4.1. General results

The main result from this study is that the full dataset of intermediate and deep events features Θ values generally higher than their shallow counterparts, with the difference in their averages, -4.69 and -5.10, amounting to 0.41 logarithmic units or in rough numbers a factor of 2.5 in the strain release E^E/M_0, and taking into account the increase in elastic constants with depth, a factor of five in apparent stress τ_a. Note that the average Θ for the whole I-D dataset, -4.69, is in excellent agreement with Vassiliou and Kanamori's (1982) values ($<\Theta> = -4.65 \pm 0.51$; their Table 2), even though their measurements used a different algorithm, estimating the total duration of the source, rather than integrating the recorded seismograms. In addition, the I-D dataset is relatively homogeneous, with a standard deviation of 0.29, significantly smaller than the difference quoted above between shallow and I-D datasets, and than the standard deviation for shallow earthquakes (0.55). This does not preclude the existence of heterogeneity in the slabs, but on a smaller scale than for shallow earthquakes: with the exception of one outlier at the upper limit of the Solomon Islands subduction system (see below), the Θ dataset for I-D sources covers a range of 1.95 logarithmic units, as compared to 3.10 for shallow events.

When I-D is split into its four depth bins, a slight increase of Θ with depth can be detected, but all four one-σ bands share a common interval, ranging from -4.56 to -4.74. By contrast, the reference shallow dataset has an average Θ of -5.10, falling outside all four I–D bands, and a much larger standard deviation, $\sigma_s = 0.55$, more than twice that of all individual I-D bins.

When further splitting the shallow dataset into interplate and intraplate events, we confirm the generally higher Θ values of the latter, as already described by Okal and Kirby (2002) and Choy and Kirby (2004); we find that the mean and standard deviation of the intraplate values of Θ (-4.68 ± 0.33) are fully comparable to those of the I-D dataset, or for that matter of any of its depth bins, especially the two intermediate ones. This implies that the generally higher values of Θ for I-D events are rooted in their intraplate nature, rather than in the greater source depth. By contrast, the generally lower values observed for interplate shallow sources express a difference between conditions at the interplate contact and within a single plate, with the larger scatter in Θ featured by shallow interplate events being tied to the lateral heterogeneity in those conditions; we stress however that the

Table 3
Values of Θ for specific events or subsets.

Events	Date	Epicenter		Depth	Θ	σ
	D M (JJJ) Y	(N°)	(E°)	(km)		
		Regional Subsets				
Hindu Kush	19 events	≈ 36.5	≈ 70.5	182–254	−4.57	0.22
Burma	4 events	19–25	≈ 95	86–150	−4.64	0.24
Tonga (D-2)	78 events	−31 to −17	178–183	453–699	−4.41	0.23
Tonga (all depths)	147 events	−31 to −17	178–183	83–699	−4.56	0.28
		Individual Events				
O_1 Solomon Is.	09 SEP (252) 2005	−5.20	153.95	84	−5.92	
Vrancea*	31 MAY (151) 1990	45.67	26.00	87	−4.90	
Bucaramanga	10 MAR (069) 2015	6.83	−73.11	156	−4.61	
Fiji Basin	13 APR (103) 1995	−13.34	170.71	646	−4.59	
Fiji Basin	05 MAR (064) 2014	−14.64	169.80	661	−4.76	
		Largest Deep Shocks ($M_0 > 5 \times \mathbf{10}^{27} dyn^{*}cm$)				
Bolivia	09 JUN (160) 1994	−13.82	−67.25	647	−3.85	
Flores Sea	17 JUN (169) 1996	−7.38	123.02	584	−4.56	
Sea of Okhotsk	24 MAY (144) 2013	54.61	153.77	611	−4.01	
Bonin Islands	30 MAY (150) 2015	27.94	140.56	681	−4.20	

* Fewer than 10 stations; not part of standard dataset.

geographical distribution of shallow interplate outliers, featuring extreme values of Θ, and notably that of the so-called "tsunami earthquakes", has yet to be modeled in the context of simple tectonic parameters such as lithospheric age or plate kinematics.

In Table 1, we further examine the effect, on our results, of imposing a minimum number N_{min} of stations (we recall that the standard dataset uses $N_{min} = 10$). The second group in the table imposes no such minimum, while the third one raises N_{min} to 20. In all cases, the average values of Θ vary by at most a few hundredths of one logarithmic unit. Most remarkably, even the group of 93 earthquakes for which fewer than ten stations were available (last group in Table 1) features, in all bins, average values of Θ falling inside the relevant one-σ band of the standard dataset (that class of earthquakes consists primarily of events from the early 1990s, when the Global Seismic Network was still under development). This experiment underscores the robustness of the concept of the parameter Θ.

On Fig. 8, we investigate any possible trend between Θ and earthquake size, by attempting a regression against $\log_{10} M_0$. Any such trend could be the sign of a putative systematic error, potentially traceable to approximations in our methodology (*e.g.*, the selection of t_{max}). We find no such evidence, with both an insignificant slope (0.06) and a poor correlation between the two quantities (14%). This can also be expressed as a slope of 1.06 when regressing $\log_{10} E^E$ *vs.* $\log_{10} M_0$.

4.2. Possible influence of focal mechanism

We further investigate the I-D dataset by researching any possible dependence of Θ on focal mechanism. We are motivated by the fact that Choy and Boatwright (1995) have suggested that strike-slip earthquakes feature higher energy-to-moment ratios than those with other mechanisms, although NO98 pointed out a possible bias due to over-correction for strike-slip radiation patterns which could be affected by uncertainties in focal geometry or lateral heterogeneity at the source, and by the expected break-down in scaling laws for strike-slip sources reaching faster saturation of their fault width W, on account of their steeper fault dips. Choy et al.'s (2006) later study, which addressed those reservations, generally supported their initial results, and further indicated a variation in apparent stress (closely related to Θ) with tectonic characteristics of shallow earthquakes such as lithospheric strength and fault maturity. Pérez-Campos and Beroza (2001) also suggested a weak dependence of radiated energy on focal mechanism. In this context, it seems justified to explore any possible variation of Θ with focal geometry in the I-D dataset.

For this purpose, we sort the dataset using the concept of ternary diagrams introduced by Frohlich and Apperson (1992). We recall that, based on the remark that the three dip angles of the principal axes T, B, P of any double-couple satisfy $\sin^2\delta_T + \sin^2\delta_B + \sin^2\delta_P = 1$, these authors proposed that any such mechanism can be regarded as a barycentric combination of Strike-Slip (SS), Normal (NO) and Thrust (TH) mechanisms, which they plot inside an equilateral triangle with "pure" mechanisms at the apices.[1]

Here, we define events as SS, NO, or TH if they have dips δ_B, δ_P or δ_T respectively, satisfying $\sin^2\delta \geqslant 2/3$ (or $\delta \geqslant 54.75°$), this angle being chosen as the complement of the common dip angle of the three axes of a mechanism plotting at the center of the ternary diagram (Frohlich and Apperson, 1992). We call other events Hybrid (HY). This is a more symmetric definition than Frohlich and Apperson's (1992), who allowed a shallower dip (50°) for TH, as opposed to SS and NO (60°). Under our conventions, a randomly oriented double couple has an equal 18% chance of being classified as SS, NO or TH, and a 45% chance as HY, compared with 14%, 14%, 23%, and 49%, respectively under Frohlich's.

Fig. 9 plots the resulting ternary diagrams for the four depth bins, and Table 2 lists the new statistics for the resulting 16 sub-datasets. The population disparity between various classes illustrates partly the greater probability of an HY orientation, and partly the consistency of stresses released by deep earthquakes, as initially pointed out in Isacks and Molnar's (1971) landmark study: for example, the deepest earthquakes in bin D-2 are expected to be down-dip compressional as the slab abuts against the more viscous deep mantle, which results in an NO mechanism for steeply sinking slabs, and a dip-slip on a vertical fault (HY) for a shallower dip. Note that we identify only one strike-slip D −1 event, and therefore this category has no standard deviation. With the possible exception of that one event, which bears no statistical significance, we find no robust variation with focal mechanism in average Θ or standard deviation in any of the four depth bins.

A limitation of the above study is that stresses in descending slabs are controlled by the 3-D kinematics of the subduction, and the nature (TH, NO, SS or HY) of a particular mechanism should be described in an

---

[1] We correct a typographic error in Frohlich and Apperson (1992, p. 285), later reproduced in Frohlich (1992, p. 195). The denominator common to the two lines of Eq. (15) should read

$$\sin(35.26°)\,\sin\delta_B + \cos(35.26°)\,\cos\delta_B\,\cos\psi$$

.

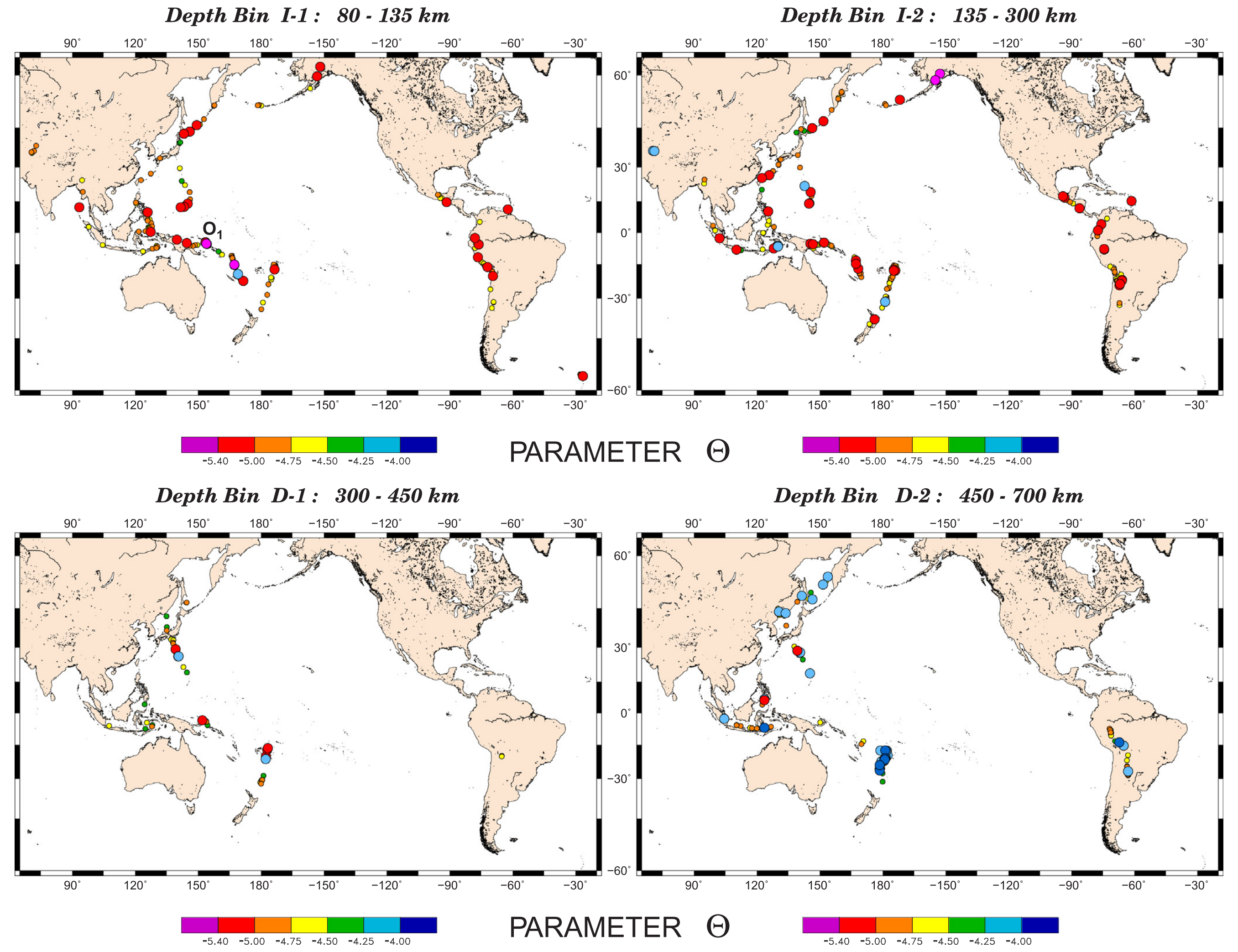
Depth Bin I-1 : 80 - 135 km

Depth Bin I-2 : 135 - 300 km

Depth Bin D-1 : 300 - 450 km

Depth Bin D-2 : 450 - 700 km

PARAMETER Θ

Fig. 11. Maps of the dataset of 598 intermediate and deep earthquakes, separated in the 4 depth bins and color-coded according to Θ. To avoid clutter, events with average values ($-5.00 < \Theta < -4.25$) are shown with smaller symbols. See text for discussion.

appropriately rotated frame where the vertical axis is taken as the normal to the Wadati-Benioff plane. On Fig. 10, we perform such a rotation for the 147 events located in the Tonga-Kermadec subduction system, which offers sufficiently abundant seismicity to allow significant conclusions. We define the slab as striking N20°E, and dipping 45° North of 27°S and 60° farther South (Sykes, 1966). Fig. 10 shows that the majority of I–D earthquakes in Tonga-Kermadec take place in Depth Bin D-2, at the bottom of the slab, where it abuts against the lower mantle, and feature a down-dip compressional axis (an observation going back to Isacks and Molnar (1971)). Such events are either classified as TH in the slab geometry, when their null axis is subhorizontal, parallel to the strike of the slab, SS when their T axis takes that orientation, of HY in between. At any rate, the average value of Θ varies insignificantly between the four geometries. At lesser depths, the datasets are much sparser, and as such do not lend themselves to meaningful interpretation, with the possible exception of Depth Bin I–2, where we tentatively recognize a group of down-dip tensional events (“normal”), and a group of down-dip compressional ones (“thrust”) which could correspond to bending stresses in different layers of the slab; again, we find no significant difference in populations of Θ between the two geometries. We conclude that, even when referred to coordinates defined in the geometry of the subducting slab, focal mechanism has no perceptible effect on the populations of Θ.

We interpret this result once again as an expression of probable structural homogeneity of the intra-slab seismogenic zones. In Choy et al.’s (2006) model, variations in Θ for shallow earthquakes are ascribed to differences in the properties of the relevant faults, such as their inter- or intra-plate character or their degree of maturity. Because in turn these conditions often dictate the focal geometry (e.g., interplate subduction gives rise to thrust mechanisms), a correlation can be found between Θ and focal mechanism. For I-D events, our study suggests that the mechanical properties of the faults supporting rupture are homogenized, probably as a result of the pressure and thermal evolution of the slab material during its long descent into the mantle. In particular, they will not reflect the orientation of the faults (which may or may not correspond to reactivation of subducted shallow faults) that will eventually control the focal geometry.

4.3. Regional trends, outliers and special groups

We examine below in more details a number of subgroups or regions of particular interest. All relevant numbers are compiled in Table 3.

While the I-D dataset is generally more homogeneous than its shallow counterpart, it does feature a clear outlier in Depth Bin I–1, identified by a bull’s eye symbol and labeled “O_1” on Fig. 3. This large event ($M_0 = 3.7 \times 10^{27}$ dyn∗cm) took place on 09 September 2005 in the Solomon Islands subducting slab at a depth of 84 km, and featured an extremely slow value of $\Theta = -5.92$, comparable to those of tsunami earthquakes. In this respect, it is reminiscent of the large earthquake of 31 December 1966 in Santa Cruz ($h = 78$ km; $M_0 = 4 \times 10^{27}$ dyn∗cm),

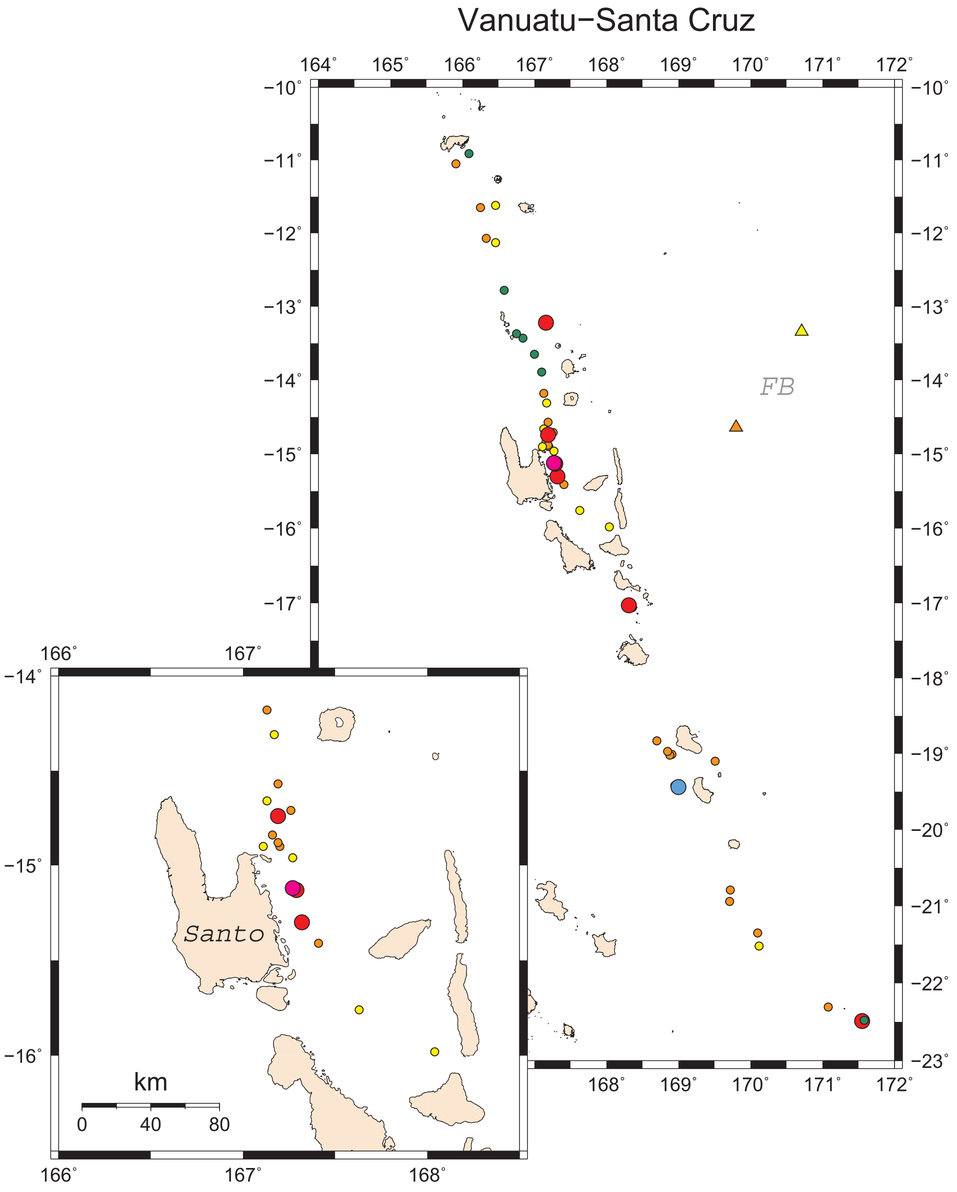

Fig. 12. Close-up of the results in the Vanuatu-Santa Cruz region. Symbols as on Fig. 11. The inset at lower left zooms on the island of Santo, Northern Vanuatu. Note the four earthquakes trending towards slowness (red and magenta symbols, $\Theta < -5.00$) at the exact same latitude as slow shallow events documented by Okal and Saloor (2017). The two triangles denote D–2 earthquakes belonging to the deep Fiji Basin (FB) cluster.

for which Okal and Saloor (2017) have proposed a comparable value of Θ (-5.83) suggesting that anomalous conditions leading to source slowness in shallow earthquakes may occasionally persist across the classical boundary between shallow and intermediate earthquakes.

Next, we examine on Fig. 11 the geographic distribution of our results, color-coded according to Θ . In order to minimize clutter, we split the data into the four depth bins, and we represent those events with intermediate values of Θ (between -5.00 and -4.25) with smaller symbols, electing to focus on those trending towards deficient Θ (< -5.00; red or magenta), or enhanced Θ (> -4.25; light or dark blue). Fig. 11 does not reveal any systematic large scale geographic pattern in the diversity of Θ values in any of the four depth bins.

The deep (D – 2) dataset in Tonga-Kermadec is of particular interest, given the extreme thermal parameter Φ (product of age at subduction by rate of vertical descent (Kostoglodov, 1989; Kirby et al., 1991)) of this subduction system where old, Cretaceous lithosphere plunges at unparalleled converging rates, thus preserving an exceptionally cold field of temperatures in the deepest part of the slab. Okal and Kirby (1995) showed that this led to a distinct pattern of frequency-size relations; the question then arises naturally whether a distinct trend in Θ may also be present. For the 78 Tonga-Kermadec events deeper than 450 km, and including all focal geometries, we find $\langle\Theta\rangle = -4.41 \pm 0.23$, again not significantly different from the global average value (-4.48 ± 0.26) for the D – 2 bin. Similar results are found in the other depth bins (I–1: 14 events, -4.78 ± 0.20; I–2: 36 events, -4.71 ± 0.20; D–1: 19 events, -4.70 ± 0.29). We conclude that the exceptional thermal conditions in the Tonga slab have no effect on Θ, regardless of depth.

In Fig. 12, we zoom on the results for the Vanuatu-Santa Cruz subduction zone, for which Okal and Saloor (2017) have documented a strong diversity in Θ at shallow depths, possibly correlating with the level of coupling of the subduction. We similarly note four slow events (magenta and red symbols; $\Theta = -5.13, -5.21, -5.30, -5.46$) off the central part of Santo, where Okal and Saloor (2017) identified anomalously slow earthquakes, including a documented tsunami earthquake, among the 1965 aftershock series. However, this possible similarity takes places next to a zone of strong diversity in Θ immediately to the North, and may just be fortuitous.

Fig. 12 also includes two earthquakes, shown as triangles, belonging to the deep Fiji Basin (FB) group, interpreted by Okal and Kirby (1998) as located in a remnant piece of the fossil Vityaz slab, now lying recumbent at the bottom of the transition zone. Because this piece of slab is mechanically detached from any convection cell, its state of stress may be singular; however the values of Θ for those two lone events

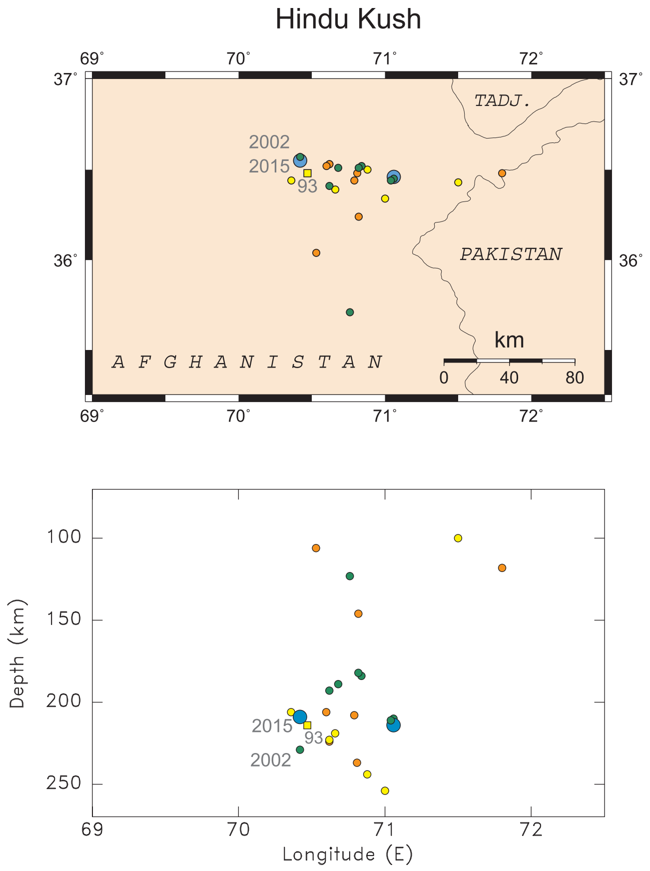

Fig. 13. *Top*: Map of our results for the Hindu Kush cluster using the same symbols as on Figs. 11 and 12. Events studied by Zhan and Kanamori (2016) are identified, with the 1993 one shown as a square. *Bottom*: East–west cross-section of the dataset; no vertical exaggeration.

(-4.53 and -4.68) fit within the one-σ band for the D – 2 bin.

We next consider the case of the Hindu Kush. This region features an intriguing nest of abundant, occasionally strong intermediate depth seismicity, with most large events ($M \geqslant 6$) clustering in a volume not exceeding 150 km in all three dimensions, although detailed studies of lower-level seismicity have proposed (Nowroozi, 1971) and later documented (Khalturin et al., 1977) a system of continuous Wadati-Benioff zones now believed to involve a lateral change of subduction polarity (Sippl et al., 2013). Our dataset comprises 24 events in the Hindu-Kush, 19 of which in a compact Southern cluster at depths of 182 to 254 km. They are shown in map view and cross-section on Fig. 13 with the same symbols as on Fig. 11. For this group, we find $\langle\Theta\rangle = -4.57 \pm 0.22$, on average slightly higher than for the entire I – 2 family, but within its one-σ band (-4.77 ± 0.22).

Zhan and Kanamori (2016) have studied three recent large earthquakes from the Hindu Kush cluster and shown that even though they shared a common hypocenter and focal mechanism, they differed significantly in terms of source duration, rise time and precursory signals. They identified the event of 03 March 2002 as featuring a very short duration (less than 10 s for a moment of 1.3×10^{27} dyn∗cm), while the larger earthquake of 26 October 2015 ($M_0 = 2.2 \times 10^{27}$ dyn∗cm) did show more source complexity; their third and smaller event (09 August 1993 (12:42), $M_0 = 3.6 \times 10^{26}$ dyn∗cm) had a very complex time history with a source lasting 20 s. We obtained Θ values of -4.45 in 2002, -4.19 in 2015 and -4.57 in 1993. Note that the first two events fall outside the one-σ band of the whole I – 2 depth bin, and that the third earthquake is not part of the standard dataset, as only 9 stations were available; we have added it as a square on Fig. 13. We find no resolvable trend between source complexity, as evidenced by Zhan and Kanamori (2016); however the dataset is clearly too small to draw any definitive conclusion.

We similarly examine the subset of intermediate-depth (I – 1 and I – 2) events in Myanmar (*ex*-Burma), mainly clustered around 24°N, 95°E and arguably an Eastern, but shallower and less active, counterpart to the Hindu Kush system. Based on a meager number of events (4), we find a mean value ($\langle\Theta\rangle = -4.64$) comparable to that of the Hindu Kush cluster.

Other areas of potential interest would include Vrancea, Romania (I – 1), and the Bucaramanga, Colombia nest (I – 2). Unfortunately, our dataset includes only one event for each of those provinces, both of them featuring regular values of Θ for their respective depth bins.

Finally, we examined four deep (D – 2) mega-events, defined as having a moment exceeding 5×10^{27} dyn∗cm. We find generally high values of Θ for the 1994 Bolivian, 2013 Okhotsk and 2015 Bonin earthquakes (-3.85, -4.10 and -4.20, respectively), and an average one (-4.56) for the 1996 Flores Sea event.

For the 2013 Sea of Okhotsk earthquake, this translates to an estimated energy $E^E = 3 \times 10^{17}$ J, or twice the value proposed by Ye et al. (2013), but within their claimed factor of uncertainty. We do not find a striking difference in Θ between the 2013 mainshock and its aftershock at 14:56 GMT, for which we note that Ye et al. (2013) use only half the moment value listed in the GlobalCMT catalog. Both events would qualify as “snappy”, in agreement with short durations and fast rupture velocities. The values listed in the National Earthquake Information Center’s Preliminary Determinations of Earthquake Bulletins (9.4×10^{16} and 8.8×10^{14} J, respectively) are significantly smaller than Ye et al.’s (2013).

Regarding the 1994 Bolivian earthquake, our proposed Θ, obtained on a dataset of 10 stations, yields an estimated energy of 3×10^{17} J, about a factor of 6 more than quoted by Ye et al. (2013), from Winslow and Ruff (1999). We note however that these authors considered attenuation as “unimportant”; even a low average t^* of 0.3 s would compensate for that factor in the frequency range 0.5–1 Hz. The significant difference between our estimated energy and the value proposed by the NEIC PDE (3.2×10^{16} J) may reflect a difference in t_{max} for this event featuring a long duration (about 50 s) and a strong source complexity (Lundgren and Giardini, 1995; Chen, 1995).

In the case of the intriguing 2015 Bonin Islands earthquake, which took place roughly 100 km deeper than previously known seismicity in that subduction system, we obtain $E^E = 4.8 \times 10^{16}$ J, within a factor of 2 of Ye et al.’s (2016) estimate (3.3×10^{16} J). Finally, for the 1996 Flores event, our estimated energy ($E^E = 2.0 \times 10^{16}$ J) is in excellent agreement with the NEIC PDE estimate ($E^E = 1.8 \times 10^{16}$ J), but again significant larger than Winslow and Ruff’s (1999).

5. Conclusion

We have derived algorithms to extend the computation of the slowness parameter Θ to intermediate and deep earthquakes, and successfully applied them to a global dataset of close to 600 earthquakes. While we document a slight increase of Θ with depth, the most significant aspect of our results is the consistency of the Θ values, which feature a global standard deviation of only 0.31 logarithmic units, as compared to 0.55 units for a reference dataset of 146 shallow earthquakes. This relative constancy of Θ values, shared by shallow intraplate events, suggests a lack of large scale heterogeneity in the state of stress inside the seismogenic zones of slabs, in contrast to the case of shallow interplate earthquakes, for which a diversity of tectonic environments can lead to a greater variability of stresses, and hence of Θ values. Similarly, we found no correlation between Θ and the focal geometry of intermediate and deep earthquakes, which suggests that while the latter generally reflects the orientation of ambient stresses controlled by the local dynamics of subduction, the amplitude of apparent stresses remains unaffected by their geometry.

While differences may persist regarding the detailed thermal regime of subducting slabs, controlled by convergence rate and lithospheric age at subduction, the emerging picture is that of a largely homogeneous field of stresses inside the downgoing slabs, once they have departed the more diverse boundary layer at the surface of the Earth.

Acknowledgments

We thank two anonymous reviewers for their constructive comments which significantly improved an earlier version of the manuscript. We are grateful to George Choy for directing us to the rather concealed directory of the NEIC webserver, holding the very valuable radiated energy values that he compiled over the years. Some figures were drafted using the GMT software (Wessel and Smith, 1991).

Appendix A. Supplementary data

Supplementary data associated with this article can be found, in the online version, athttp://dx.doi.org/10.1016/j.pepi.2017.10.006.

References

Anderson, D., Given, J., 1982. Absorption band Q model for the Earth. J. Geophys. Res. 87, 3893–3904.

Anderson, D.L., Hart, R., 1978. Attenuation models of the Earth. Phys. Earth Planet. Inter. 16 (4), 289–306.

Beavan, J., Fielding, E., Motagh, M., Samsonov, S., Donnelly, N., 2011. Fault location and slip distribution of the 22 February 2011 $M_w = 6.2$ Christchurch, New Zealand, earthquake from geodetic data. Seismol. Res. Lett. 82 (6), 789–799.

Boatwright, J., Choy, G.L., 1986. Teleseismic estimates of the energy radiated by shallow earthquakes. J. Geophys. Res.: Solid Earth 91 (B2), 2095–2112.

Burdick, L., Helmberger, D., 1974. Time functions appropriate for deep earthquakes. Bull. Seismol. Soc. Am. 64 (5), 1419–1427.

Carpenter, E., 1965. Attenuation of teleseismic body waves. Nature 207, 745–746.

Chen, W.-P., 1995. En échelon ruptures during the great Bolivian earthquake of 1994. Geophys. Res. Lett. 22 (16), 2261–2264.

Choy, G.L., Boatwright, J.L., 1995. Global patterns of radiated seismic energy and apparent stress. J. Geophys. Res.: Solid Earth 100 (B9), 18205–18228.

Choy, G.L., Cormier, V.F., 1986. Direct measurement of the mantle attenuation operator from broadband P and S waveforms. J. Geophys. Res.: Solid Earth 91 (B7), 7326–7342.

Choy, G.L., Dewey, J.W., 1988. Rupture process of an extended earthquake sequence: Teleseismic analysis of the Chilean earthquake of March 3, 1985. J. Geophys. Res.: Solid Earth 93 (B2), 1103–1118.

Choy, G.L., Kirby, S.H., 2004. Apparent stress, fault maturity and seismic hazard for normal-fault earthquakes at subduction zones. Geophys. J. Int. 159 (3), 991–1012.

Choy, G.L., McGarr, A., Kirby, S.H., Boatwright, J., 2006. An overview of the global variability in radiated energy and apparent stress. Am. Geophys. Un. Geophys. Monog. 170, 43–57.

Dziewonski, A., Chou, T.-A., Woodhouse, J., 1981. Determination of earthquake source parameters from waveform data for studies of global and regional seismicity. J. Geophys. Res.: Solid Earth 86 (B4), 2825–2852.

Ebeling, C.W., Okal, E.A., 2012. An extension of the E/M_0 tsunami earthquake discriminant Θ to regional distances. Geophys. J. Int. 190 (3), 1640–1656.

Ekström, G., Nettles, M., Dziewoński, A., 2012. The GlobalCMT project 2004–2010: Centroid-moment tensors for 13,017 earthquakes. Phys. Earth Planet. Inter. 200, 1–9.

Frohlich, C., 1992. Triangle diagrams: ternary graphs to display similarity and diversity of earthquake focal mechanisms. Phys. Earth Planet. Inter. 75 (1–3), 193–198.

Frohlich, C., 2006. Deep Earthquakes. Cambridge University Press 573 p.

Frohlich, C., Apperson, K.D., 1992. Earthquake focal mechanisms, moment tensors, and the consistency of seismic activity near plate boundaries. Tectonics 11 (2), 279–296.

Fukao, Y., Kikuchi, M., 1987. Source retrieval for mantle earthquakes by iterative deconvolution of long-period P-waves. Tectonophysics 144 (1–3), 249–269.

Geller, R.J., 1976. Scaling relations for earthquake source parameters and magnitudes. Bull. Seismol. Soc. Am. 66 (5), 1501–1523.

Isacks, B., Molnar, P., 1971. Distribution of stresses in the descending lithosphere from a global survey of focal-mechanism solutions of mantle earthquakes. Rev. Geophys. 9 (1), 103–174.

Kanamori, H., 1972. Mechanism of tsunami earthquakes. Phys. Earth Planet. Inter. 6 (5), 346–359.

Khalturin, V., Rautian, T., Molnar, P., 1977. The spectral content of Pamir-Hindu Kush intermediate depth earthquakes: evidence for a high-Q zone in the upper mantle. J. Geophys. Res. 82, 2931–2943.

Kirby, S.H., Durham, W.B., Stern, L.A., 1991. Mantle phase changes and deep-earthquake faulting in subducting lithosphere. Science 252 (5003), 216–225.

Kostoglodov, V., 1989. Maximum depth of earthquakes and phase transformation within the lithospheric slab descending in the mantle, Physics and Interior Structure of the Earth. Nauka, Moscow, pp. 52–57 (in Russian).

López, A.M., Okal, E.A., 2006. A seismological reassessment of the source of the 1946 Aleutian tsunami earthquake. Geophys. J. Int. 165 (3), 835–849.

Lundgren, P., Giardini, D., 1995. The June 9 Bolivia and March 9 Fiji deep earthquakes of 1994: I. Source processes. Geophys. Res. Lett. 22 (16), 2241–2244.

Newman, A.V., Okal, E.A., 1998. Teleseismic estimates of radiated seismic energy: the E/M_0 discriminant for tsunami earthquakes. J. Geophys. Res. 103, 26885–26898.

Nowroozi, A.A., 1971. Seismo-tectonics of the Persian plateau, Eastern Turkey, Caucasus, and Hindu-Kush regions. Bull. Seismol. Soc. Am. 61 (2), 317–341.

Okal, E.A., 1992. A student's guide to teleseismic body wave amplitudes. Seismol. Res. Lett. 63 (2), 169–180.

Okal, E.A., Kirby, S.H., 1995. Frequency-moment distribution of deep earthquakes; implications for the seismogenic zone at the bottom of slabs. Phys. Earth Planet. Inter. 92 (3–4), 169–187.

Okal, E.A., Kirby, S.H., 1998. Deep earthquakes beneath the Fiji Basin, SW Pacific: Earth's most intense deep seismicity in stagnant slabs. Phys. Earth Planet. Inter. 109 (1), 25–63.

Okal, E.A., Kirby, S.H., 2002. Energy-to-moment ratios for damaging intraslab earthquakes; preliminary results on a few case studies. The Cascadia subduction zone and related subduction systems–Seismic structure, intraslab earthquakes and processes, and earthquake hazards, pp. 117–121.

Okal, E.A., Saloor, N., 2017. Historical tsunami earthquakes in the Southwest Pacific: an extension to $\Delta > 80°$ of the energy-to-moment parameter Θ. Geophys. J. Int. 210 (2), 852–873.

Orowan, E., 1960. Mechanism of seismic faulting. Geol. Soc. Am. Memoirs 79, 323–346.

Pérez-Campos, X., Beroza, G.C., 2001. An apparent mechanism dependence of radiated seismic energy. J. Geophys. Res.: Solid Earth 106 (B6), 11127–11136.

Polet, J., Kanamori, H., 2000. Shallow subduction zone earthquakes and their tsunamigenic potential. Geophys. J. Int. 142 (3), 684–702.

Poli, P., Prieto, G.A., 2016. Global rupture parameters for deep and intermediate-depth earthquakes. J. Geophys. Res.: Solid Earth 121 (12), 8871–8887.

Roth, E.G., Wiens, D.A., Dorman, L.M., Hildebrand, J., Webb, S.C., 1999. Seismic attenuation tomography of the Tonga-Fiji region using phase pair methods. J. Geophys. Res.: Solid Earth 104 (B3), 4795–4809.

Sippl, C., Schurr, B., Yuan, X., Mechie, J., Schneider, F., Gadoev, M., Orunbaev, S., Oimahmadov, I., Haberland, C., Abdybachaev, U., et al., 2013. Geometry of the Pamir-Hindu Kush intermediate-depth earthquake zone from local seismic data. J. Geophys. Res.: Solid Earth 118 (4), 1438–1457.

Sykes, L.R., 1966. The seismicity and deep structure of island arcs. J. Geophys. Res. 71 (12), 2981–3006.

Tanioka, Y., Ruff, L., Satake, K., 1997. What controls the lateral variation of large earthquake occurrence along the Japan Trench? Island Arc 6 (3), 261–266.

Vallée, M., 2013. Source time function properties indicate a strain drop independent of earthquake depth and magnitude. Nat. Commun. 4, 2606 6 p.

Vassiliou, M., Kanamori, H., 1982. The energy release in earthquakes. Bull. Seismol. Soc. Am. 72 (2), 371–387.

Weinstein, S.A., Okal, E.A., 2005. The mantle magnitude M_m and the slowness parameter Θ: Five years of real-time use in the context of tsunami warning. Bull. Seismol. Soc. Am. 95 (3), 779–799.

Wessel, P., Smith, W.H.F., 1991. Free software helps map and display data. Eos, Transactions American Geophysical Union 72 (41) 441 and 445–446.

Winslow, N.W., Ruff, L.J., 1999. A hybrid method for calculating the radiated wave energy of deep earthquakes. Phys. Earth Planet. Inter. 115 (3), 181–190.

Wu, F.T., 1966. Part I: Lower limit of the total energy of earthquakes and partitioning of energy among seismic waves. Part II: Reflected waves and crustal structures (Ph.D. thesis), California Institute of Technology.

Wyss, M., Molnar, P., 1972. Source parameters of intermediate and deep focus earthquakes in the Tonga arc. Phys. Earth Planet. Inter. 6 (4), 279–292.

Ye, L., Lay, T., Kanamori, H., Koper, K.D., 2013. Energy release of the 2013 $M_w = 8.3$ Sea of Okhotsk earthquake and deep slab stress heterogeneity. Science 341 (6152), 1380–1384.

Ye, L., Lay, T., Zhan, Z., Kanamori, H., Hao, J.-L., 2016. The isolated 680 km deep 30 May 2015 $M_w = 7.9$ Ogasawara (Bonin) Islands earthquake. Earth Planet. Sci. Lett. 433, 169–179.

Zhan, Z., Kanamori, H., 2016. Recurring large deep earthquakes in Hindu Kush driven by a sinking slab. Geophys. Res. Lett. 43 (14), 7433–7441.